The origin of graben and ridges in Rachmaninoff, Raditladi, and Mozart basins, Mercury

David M. Blair,[1] Andrew M. Freed,[1] Paul K. Byrne,[2] Christian Klimczak,[2]
Louise M. Prockter,[3] Carolyn M. Ernst,[3] Sean C. Solomon,[2,4] H. Jay Melosh,[1]
and Maria T. Zuber[5]

[1]   The Rachmaninoff, Raditladi, and Mozart peak-ring impact basins on Mercury display a distinctive pattern of tectonic features consisting of a central zone that is either devoid of tectonic landforms or contains small ridges, a medial annulus of prominent and predominantly circumferentially oriented graben, and a distal zone displaying graben that occur in a mix of orientations and that are less evident toward the peak ring. Here we use finite element models to explore three candidate scenarios for the formation of these tectonic features: (1) thermal contraction of the interior smooth plains, (2) isostatic uplift of the basin floor, and (3) subsidence following volcanic loading. Our results suggest that only thermal contraction can account for the observed pattern of graben, whereas some combination of subsidence and global contraction is the most likely explanation for the central ridges in Rachmaninoff and Mozart. Thermal contraction models, however, predict the formation of graben in the centermost region of each basin, where no graben are observed. We hypothesize that graben in this region were buried by a thin, late-stage flow of plains material, and images of partially filled graben provide evidence of such late-stage plains emplacement. These results suggest that the smooth plains units in these three basins are volcanic in origin. The thermal contraction models also imply a cooling unit ~1 km thick near the basin center, further supporting the view that plains-forming lavas on Mercury were often of sufficiently high volume and low viscosity to pool to substantial thicknesses within basins and craters.

1.   Introduction

[2] The most common and widespread tectonic features on Mercury are ridges and scarps interpreted to have formed by horizontal shortening of the crust and generally attributed to the global cooling and contraction of the planet's interior [e.g., *Strom et al.*, 1975; *Solomon et al.*, 2008; *Watters et al.*, 2009a]. Mariner 10 images showed evidence for extensional

features on the floor of the Caloris impact basin, the largest well-preserved impact structure on Mercury [*Strom et al.*, 1975], and several basin-scale processes have been proposed to account for the observed extension [e.g., *Dzurisin*, 1978; *Melosh and Dzurisin*, 1978; *Melosh and McKinnon*, 1988; *Watters et al.*, 2005; *Kennedy et al.*, 2008]. The MErcury Surface, Space ENvironment, GEochemistry, and Ranging (MESSENGER) spacecraft, in orbit about Mercury since March 2011, has revealed many additional impact structures that host extensional features within their interiors, ranging from the largest basins [*Watters et al.*, 2009b, 2009c] to volcanically flooded craters only a few tens of meters across [*Head et al.*, 2011; *Freed et al.*, 2012; *Klimczak et al.*, 2012; *Watters et al.*, 2012].

[3] Here we focus on extensional tectonic features within three peak-ring basins 200–300 km in diameter: Rachmaninoff, Raditladi, and Mozart. The smooth plains within the inner peak rings of these basins contain troughs interpreted to be graben (Figure 1). The graben were first imaged in Raditladi during MESSENGER's initial flyby of Mercury in 2008 [*Prockter et al.*, 2009], in Rachmaninoff during MESSENGER's third flyby in 2009 [*Prockter et al.*, 2010], and in Mozart after MESSENGER had entered orbit

[1]Department of Earth, Atmospheric, and Planetary Sciences, Purdue University, West Lafayette, Indiana, USA.
[2]Department of Terrestrial Magnetism, Carnegie Institution of Washington, NW, Washington, DC, USA.
[3]The Johns Hopkins University Applied Physics Laboratory, Laurel, Maryland, USA.
[4]Lamont-Doherty Earth Observatory, Columbia University, Palisades, New York, USA.
[5]Department of Earth, Atmospheric, and Planetary Sciences, Massachusetts Institute of Technology, Cambridge, Massachusetts, USA.

Corresponding author: D. M. Blair, Department of Earth, Atmospheric, and Planetary Sciences, Purdue University, 550 Stadium Mall Drive, West Lafayette, Indiana 47905, USA. (dblair@purdue.edu)
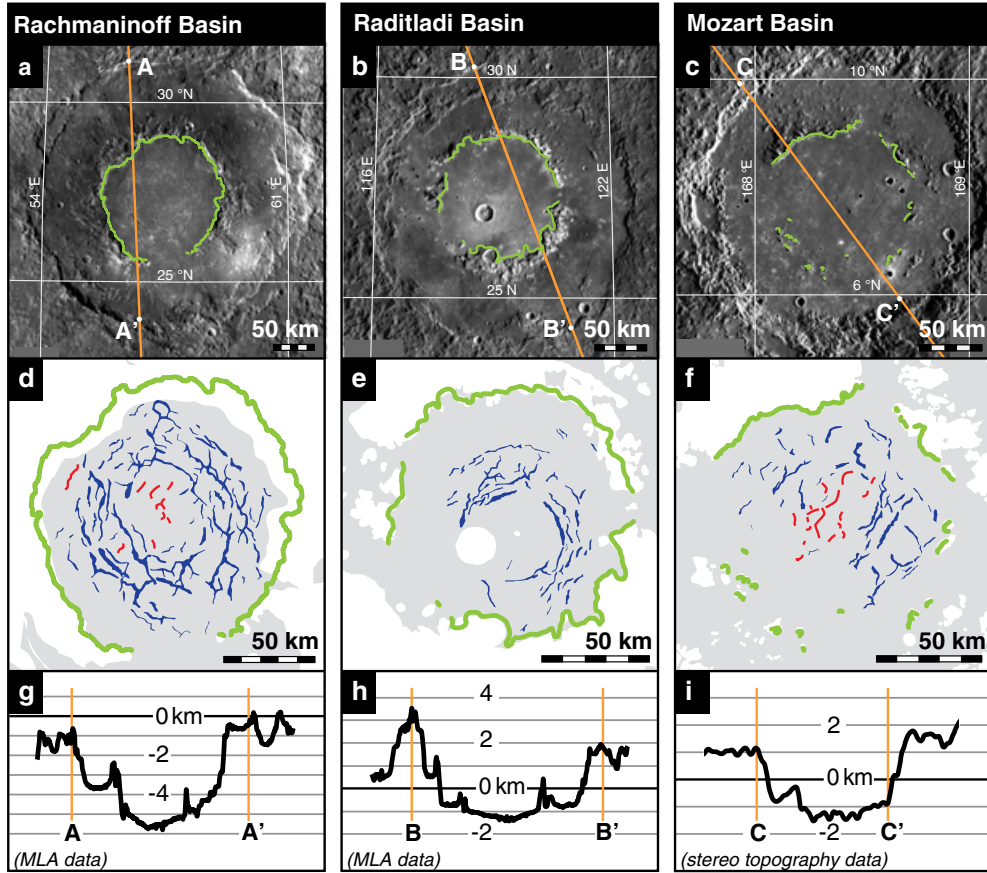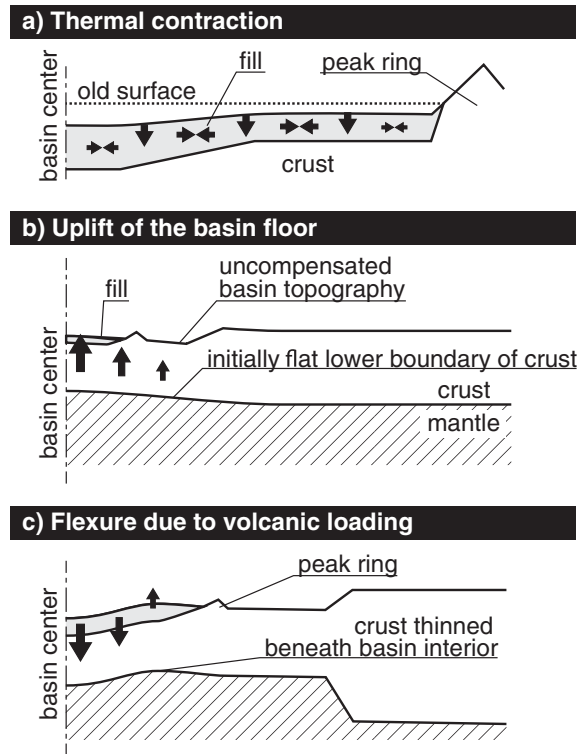
Figure 1. The Rachmaninoff, Raditladi, and Mozart peak-ring basins on Mercury. (a–c) Mercury Dual Imaging System (MDIS) image mosaics of the three basins; these mosaics are composed primarily of wide-angle camera images at 250 m pixel^{-1} with some inset images from the narrow-angle camera at 150 m pixel^{-1} and have been adjusted for contrast. Green lines show the inner edge of the peak ring in each basin, and orange lines indicate the location of the corresponding elevation profile shown in Figures 1g–1i. (d–f) Sketch maps of tectonic features (troughs in blue and ridges in red) within the peak rings of each basin (shown in green) and their relationship to the local smooth plains unit (grey shading). The general pattern is one of a central area without graben (but with ridges in Rachmaninoff and Mozart), a surrounding medial annulus dominated by circumferential graben, and a sparser distribution of graben of mixed orientations in a distal zone. (g–h) Mercury Laser Altimeter (MLA) and (i) stereo-derived topographic profiles across each basin, with horizontal lines showing elevation with respect to a reference sphere of radius 2440 km and vertical orange lines marking the positions on the basin rims corresponding to the labeled points in (a)–(c). Note that the profiles extend past the edges of the images shown in most cases.

around Mercury [*Prockter et al.*, 2011]. In each of the three basins, the troughs are distributed in a distinctive pattern (Figure 1). Immediately outside of a central region that lacks graben (but contains small ridges in Rachmaninoff and Mozart) is a medial annulus of predominantly circumferential graben. Beyond that annular zone the density and prominence of graben generally decreases toward the peak ring, and the graben occur in a mix of circumferential, radial, and oblique orientations. No graben are evident outside the peak ring.

[4] Several mechanisms have been explored to account for extensional features within impact structures on Mercury. For volcanically buried "ghost" craters and basins in Mercury's northern plains and in the plains exterior to the Caloris basin, photogeological observations and finite-element modeling support the hypothesis that the graben formed in response to the thermal contraction of a thick flood lava unit [*Watters et al.*, 2012; *Freed et al.*, 2012]. The contraction of the cooling lava generates large extensional stresses, which can form graben if the cooling unit is sufficiently thick to support large, deep faulting instead of pervasive surficial cracking. In the northern plains, these thick cooling units typically form as a result of pooling of lava in a crater or basin. In the peak-ring basins of this study, the basin itself may provide the necessary topographic depression to favor formation of a thick cooling unit. Thermal contraction is thus a candidate contributor to the formation of the tectonic features observed in these basins (Figure 2a).

[5] Another potential mechanism for the formation of graben within an impact structure is uplift of the basin floor. Such uplift can be isostatic in nature, with an initial under-compensation of basin topography inducing uplift of the crust and mantle until isostatic forces are balanced by

a) Thermal contraction

b) Uplift of the basin floor

c) Flexure due to volcanic loading

Figure 2. Schematic illustrations of candidate mechanisms for graben formation on the floors of Rachmaninoff, Raditladi, and Mozart basins: (a) thermal contraction of an interior volcanic plains unit, (b) uplift due to isostatic readjustment following basin excavation, and (c) flexure in response to emplacement of an interior volcanic plains unit. All illustrations show an axisymmetric basin with the axis of symmetry (the basin center) at the left edge. Arrows show the direction of movement, with arrow size indicating relative magnitude of motion. Illustrations are not to scale.

topographic changes and flexural stresses (Figure 2b). Alternatively, uplift can be driven by inward flow of the lower crust in response to higher overburden pressures in the lower crust exterior to the basin [e.g., *Zhong*, 1997]. Both forms of uplift should produce surficial horizontal extensional stresses within the basin interior, and both have been invoked to account for graben formation within the Caloris basin [e.g., *Dzurisin*, 1978; *Melosh and Dzurisin*, 1978; *Watters et al.*, 2005].

[6] A third candidate mechanism for the formation of graben within an impact basin, and one that can also account for ridge formation, is lithospheric flexure in response to the deposition of volcanic material (Figure 2c). Volcanic infilling of a basin generates a surface load that induces subsidence and horizontal compression at the center of the basin and flexural uplift and extension at a distance from the basin center that depends on lithospheric thickness at the time of emplacement. This mechanism has been invoked to explain interior wrinkle ridges and graben in some large lunar mare basins [e.g., *Melosh*, 1978; *Solomon and Head*, 1979, 1980; *Freed et al.*, 2001]. These lunar basins, however, have ridges throughout their interiors and graben around their peripheries, instead of ridges (where present) confined to the center of the basin and graben only inward of

approximately half the distance to the rim as in the peak-ring basins discussed here (Figure 1).

[7] In this paper we explore these three candidate scenarios for the formation of graben and ridges in Rachmaninoff, Raditladi, and Mozart basins: (1) thermal contraction of the interior smooth plains unit, (2) uplift of the basin floor, and (3) subsidence in response to interior volcanic loading. For each mechanism, we employ finite element models to calculate the stress state that is generated within the basin, and we then compare this stress state with that implied by the observed faulting patterns. The goal of these comparisons is to identify the mechanism or combination of mechanisms that best accounts for the observed pattern of tectonic features in peak-ring basins on Mercury and the absence of similar patterns of tectonic features in other basins on Mercury and elsewhere in the Solar System.

2. Observational Constraints

[8] Rachmaninoff, Raditladi, and Mozart are midsized basins on Mercury [e.g., *Fassett et al.*, 2012] that are respectively ~290, 265, and 235 km in diameter and have generally similar basin morphologies (Figure 1). All three are classified as peak-ring basins, with peak-ring diameters of ~145, 130, and 125 km, respectively (each ~50% of the rim-to-rim diameter) [*Baker et al.*, 2011]. Each contains a smooth plains unit that fills most of the area interior to the peak ring (Figure 1). Nonetheless, there are differences among the basins in the extent (and possibly the origin) of the interior smooth plains unit and in the details of the pattern and size of tectonic features. We focus here on the features shared among the three basins to develop constraints for models of fault formation, but we also take note of the differences among the basins to inform the range of basin characteristics that a successful model must be able to accommodate.

2.1. Extent and Origin of Smooth Plains Material

[9] Smooth plains material fills much of the central area bounded by the peak ring in each of the three basins. In Rachmaninoff, the smooth plains are mostly confined to this area, but images indicate that inner floor material partially buries a portion of the southernmost sector of the peak ring [*Prockter et al.*, 2010] (Figure 1d). The smooth plains in Raditladi extend farther from the basin center than in Rachmaninoff and abut the main basin rim to the east and west (Figure 1e). In Mozart, smooth plains cover ~60% of the basin interior, burying the southwestern portion of the peak ring except for a few isolated peaks (Figure 1f). Extrapolation of depth-to-diameter ratios for craters on Mercury from data given by *Barnouin et al.* [2012] suggest that these basins may have been ~3–4 km deep at the time of their formation. Topographic profiles across each basin, obtained with MESSENGER's Mercury Laser Altimeter (MLA) (Figures 1g and 1h), show rim-to-floor depths of ~5 km in Rachmaninoff and ~4 km in Raditladi, whereas the rim-to-floor depth in Mozart is ~3 km as determined from Mercury Dual Imaging System (MDIS) stereo-derived topography (Figure 1i) [*Preusker et al.*, 2011]. (MLA profiles of Mozart as of this writing pass far from the center of the basin.) All three basins are deepest at their centers, implying that some subsidence has occurred and rendering

Table 1. Styles of Faulting Predicted From the Relative Magnitude of the Principal Stress Components[a]

Relative Magnitudes	Predicted Faulting Style
$\sigma_r > \sigma_c > \sigma_v$	Circumferential graben
$\sigma_r \approx \sigma_c > \sigma_v$	Mixed-orientation graben
$\sigma_c > \sigma_r > \sigma_v$	Radial graben
$\sigma_v > \sigma_c > \sigma_r$	Circumferential ridges
$\sigma_v > \sigma_c \approx \sigma_r$	Mixed-orientation ridges
$\sigma_v > \sigma_r > \sigma_c$	Radial ridges

[a]Stresses are defined to be positive in extension.

difficult the estimation of fill thickness from modern topographic relief.

[10] In Rachmaninoff, color differences between the inner smooth plains and the basin floor outward of the peak ring, and a size-frequency distribution of impact craters supporting a younger age for the interior smooth plains than for the outer basin floor, indicate that the smooth plains are volcanic in origin [*Prockter et al.*, 2010; *Chapman et al.*, 2012]. The fact that the smooth plains largely bury the southwestern sector of the peak ring in Mozart basin (Figure 1d) also favors a volcanic origin for this material. Although the size-frequency distribution of small impact craters does not show a resolvable age difference between the inner plains in Raditladi and other parts of the basin [*Martellato et al.*, 2010], embayment relations within Raditladi and its close geomorphologic similarity to the other two basins are at least permissive of a volcanic origin for those plains as well. Nonetheless, the possibility that the inner plains of Raditladi are solidified impact melt [*Prockter et al.*, 2009] cannot be ruled out.

2.2. Distribution and Size of Tectonic Features

[11] All three basins display a broadly similar pattern of graben (Figures 1d, 1e, and 1f). This pattern consists of a central region ~20 km in radius in which graben are absent, surrounded by a medial annulus ~5–20 km wide of prominent graben. The graben in this annulus display a predominantly basin-circumferential orientation that is expressed most strongly in Raditladi (Figure 1e) and least strongly in Mozart (Figure 1f), though a few graben in this annulus in all three basins have subradial orientations. Outside of the annulus is a distal zone with a lower density of graben displaying a mix of radial, circumferential, and oblique orientations relative to the basin center. Few graben are seen immediately inward of the peak ring. This entire pattern is offset from the basin center by ~10 km in Rachmaninoff and Raditladi, likely the result of departures from axisymmetry in basin structure. In Rachmaninoff and Mozart, the center-most region (inside the annulus of circumferential graben) contains wrinkle ridges with no apparent preferred orientation; in Raditladi, this same region contains no visible tectonic features. There are no crosscutting relationships visible between the ridges and the graben, so the relative timing of these features remains unresolved.

[12] In Rachmaninoff, the annular zone of prominent circumferential graben is found at radii of approximately 20 to 40 km from the center of the pattern of faulting (14–28% of the peak-ring radius, r_p), whereas this zone spans radial distances of 20–25 km in Raditladi (15–19% of r_p) and

25–40 km in Mozart (20–32% of r_p). The most prominent of these graben have rim-to-rim widths of ~1.5 km, a measurement that includes both the original floor width and horizontal extension on the bounding normal faults. In a few cases where floor width can be distinguished from rim-to-rim width, the floor width accounts for approximately two thirds of the total width of the graben, similar to findings for graben within ghost craters and basins in the northern smooth plains [*Klimczak et al.*, 2012]. We therefore assume that the most prominent circumferential graben generally have floor widths of ~1 km. This same two thirds approximation gives graben floor widths of ~500 m for the smallest discernable graben (near the inner edge of the peak ring). Where no graben are observed, either such features are not present or they are too small to be resolved in current MESSENGER images.

[13] It is worth noting that this pattern is different from that found in graben-bearing ghost craters and basins in Mercury's northern plains and in the plains exterior to Caloris [e.g., *Klimczak et al.*, 2012; *Freed et al.*, 2012; *Watters et al.*, 2012]. In those ghost craters and basins, which range from a few tens of kilometers to over 200 km in diameter, graben generally display wide variations in orientation and often have unorganized patterns relative to the crater or basin. Moreover, the most prominent graben in ghost craters are typically at the center of the crater [e.g., *Klimczak et al.*, 2012], instead of within an annulus having an inner radius of several tens of kilometers.

3. Modeling Approach

[14] To determine the stress state predicted by candidate mechanisms for graben and ridge formation, we developed and employed axisymmetric thermo-mechanical and visco-elastic finite element models. Because of the assumed axisymmetry of the models, we ignored the slight offset between the center of the pattern of faulting and the center of the basin in Raditladi and Rachmaninoff, and instead we assumed that the two were coincident. In all calculations, one of the principal stress directions is vertical (σ_v) because of the proximity of the free surface, and the other two are radial (σ_r) and circumferential (σ_c) to the basin by axial symmetry. The relative magnitudes of the principal stress components can be used to predict the style of faulting that should result [*Anderson*, 1951]. Table 1 provides a summary of how relative stress magnitudes translate into different faulting styles. Note that if σ_r and σ_c are approximately equal, local structural variations (e.g., heterogeneous material properties, pre-existing stress conditions, or preexisting faults) will control the orientation of any new faults. The $\sigma_r \approx \sigma_c$ stress state may also lead to a local mix of circumferential and radial orientations when faulting relieves one stress component first and leaves the other component to dominate subsequent faulting. Although this approach does not incorporate a criterion for rock strength, it has been shown that such a methodology can nonetheless predict the distribution and types of faulting observed [*Banerdt et al.*, 1992; *Freed et al.*, 2001; *Golombek and Phillips*, 2010] when lithospheric strength is included in the models [*Schultz and Zuber*, 1994; *Andrews-Hanna et al.*, 2008; *Schultz et al.*, 2010].
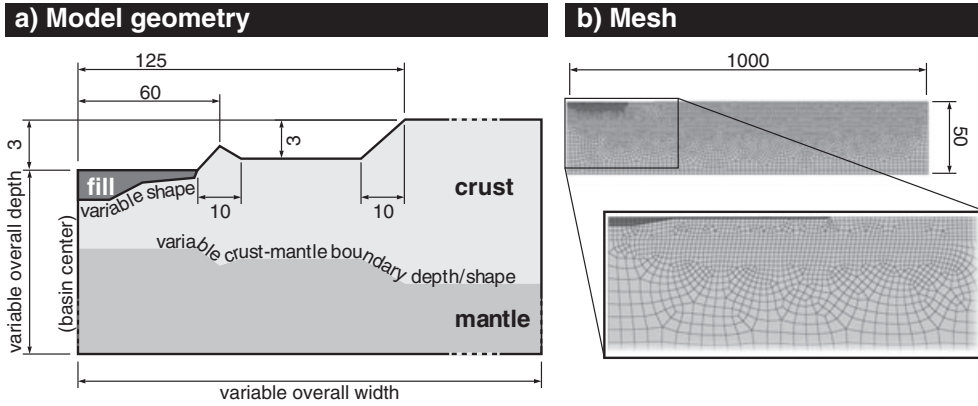
Figure 3. (a) Sketch of model geometry, not to scale, with all dimensions in kilometers. The depth and shape of the infilling smooth plains material (dark grey) and the crust-mantle boundary was varied with the mechanism being modeled. The model was 50 km deep and 500 km wide in thermal models, and 200 km deep and 1000 km wide in flexural models, with model depth measured from the floor of the basin. (b) An example mesh used in thermal contraction calculations (the darker colors at upper left are an effect of more closely spaced element boundaries). Inset shows an expanded view of the smooth plains area, with the fill unit shaded in darker grey.

[15] We used the Abaqus software suite [http://www.simulia.com/solutions], which has a substantial heritage in modeling geophysical processes [e.g., *Dyksterhuis et al.*, 2005; *Freed et al.*, 2010; *Poulet et al.*, 2012], including the generation of graben in volcanically filled craters and basins on Mercury [*Freed et al.*, 2012]. These continuum-mechanics models predict the total stress state that develops in the basin but do not simulate fault initiation, and so do not explicitly treat modification of the stress field by faulting, though we consider such effects qualitatively in later discussion.

[16] We adopted a basin radius of 125 km, the average for the three basins that have motivated this study, a peak ring with a radius of 60 km, and an initial basin depth of 3 km from rim crest to central floor to account for the fact that the basin depths determined by MLA are modern rather than original quantities. A typical model geometry is shown in Figure 3a, and variations on this geometry are discussed below. We assumed a crustal density of 3200 kg m^{-3} on the basis of a composition intermediate between basaltic and ultramafic materials [*Nittler et al.*, 2011], a density of smooth plains material that equals the crustal density on the basis of spectral evidence for broadly similar compositions [*Denevi et al.*, 2009], and a mantle density of 3400 kg m^{-3} [*Hauck et al.*, 2004]. We explored other values for these parameters, as well as for initial basin depth, and we found that although these quantities influenced stress magnitudes, they did not markedly affect the relative magnitudes of principal stresses, which is our primary focus. All models were run under an average surface gravitational acceleration of 3.7 m s^{-2}. Graben have bounding antithetic normal faults that meet at depth, so if we adopt a dip angle of 60° and assume that the graben floor does not widen with time, we may use floor width as a proxy for the minimum depth of the unit in which the graben formed [e.g., *Melosh and Williams*, 1989; *Schultz et al.*, 2007]. We thus took graben floor widths of 500 m near the basin periphery and 1 km at the basin center to imply minimum smooth plains unit thicknesses in those locations. The inclusion of smooth plains outside of the peak ring did not affect results for any of the three scenarios, so such units were not considered in the models we present here.

[17] Results were obtained after each model had run to steady state (i.e., asthenospheric viscosities had reached a completely relaxed state for uplift and subsidence models, and smooth plains material had cooled to background temperatures in the fully elastic thermal contraction models), so our choices of viscosity (10^{20} Pa s) and thermal conductivity (1.5 W m^{-1} K^{-1}) did not affect our conclusions. A summary of geometric and dynamic parameters for all models is given in Table 2. The spatial extent and mesh resolution of the models varied with the mechanism being simulated, as described in the relevant sections below. An example mesh used for a thermal contraction scenario is shown in Figure 3b.

4. Evaluation of Candidate Mechanisms

4.1. Thermal Contraction of Smooth Plains Material

[18] We modeled thermal contraction by calculating the conductive cooling of an initially hot volume of lava within a preexisting basin. The initial temperature of the lava was taken to be 800°C, the approximate elastic "blocking temperature" below which the material will accumulate thermal stresses [*Hirth*, 2002]. We assumed an ambient radiative surface temperature of 100°C [*Vasavada et al.*, 1999] and a vertical temperature gradient of 10 K km^{-1} for the surrounding basement materials [*Hauck et al.*, 2004; *Zuber et al.*, 2010] and then ran our models without the fill in place in order to establish the background thermal gradient. We then emplaced the hot lava on top of that gradient with its own surface temperature fixed at 100°C. The bottom of the model was fixed at 530°C, which we confirmed was sufficiently distant not to affect the cooling timeframe of the smooth plains. Our models for this scenario extended to a depth of 50 km and a radius of 500 km from the basin center. Our models contained zero-displacement boundary conditions on their outer and bottom edges, and we verified that

Table 2. Model Parameters

| Symbol	Description	Value	Units
ρ_c	Density of crust and smooth plains[a]	3200	kg m^{-3}
ρ_m	Density of mantle[b]	3400	kg m^{-3}
E_f, E_m	Young's modulus of fill and mantle	10^{11}	Pa
E_c	Young's modulus of crust	10^{10}	Pa
v	Poisson's ratio	0.25	
η_a	Viscosity of asthenosphere	10^{20}	Pa s
η_c	Viscosity of lower crust (lower crustal flow models only)	10^{20}	Pa s
g	Gravitational acceleration	3.7	m s^{-2}
ΔT	Thermal gradient outside of the basin[b]	10	K km^{-1}
$T_{i,f}$	Initial temperature of infilled plains[c]	900	°C
T_s	Surface temperature	100	°C
k	Thermal conductivity[d]	1.5	W m^{-1} K^{-1}
α_v	Volumetric coefficient of thermal expansion	3×10^{-5}	K^{-1}

[a]*Nittler et al.* [2011].
[b]*Hauck et al.* [2004].
[c]*Hirth* [2002].
[d]*Ahrens* [1995].

this condition did not influence the stress state within the smooth plains compared with other choices for boundary conditions. These models were purely elastic, as the time scale associated with cooling is much shorter than that of viscous relaxation.

[19] Stresses were determined at the final steady state conditions, after several tens of thousands of Earth years had passed and the smooth plains material had cooled to background temperatures. We varied both the cross-sectional shape of the smooth plains unit and the relative elastic strength of the interior plains and the basement units. This latter parameter served as a proxy for the relative yield strength of the two units, which we expect to be comparatively high in the smooth plains (whether it is of volcanic origin or solidified impact melt) and comparatively weak in the immediately underlying region of what is likely a mix of impact melt, impact-fractured material, and regolith.

[20] The relative magnitude of the stress components, and therefore the predicted style of faulting, is controlled primarily by the geometry of the smooth plains unit (Figure 4). The strength difference between the smooth plains and surrounding units has a first-order influence on the magnitude of thermal stresses, but not the relative magnitudes of the principal stresses. This statement also holds for the assumed coefficient of thermal expansion. It is important to note that although all of our thermal contraction models indicate extensional stresses in excess of 1 GPa, these figures are a function of our modeling approach and should be taken to indicate only the high potential for faulting through this mechanism. Rocks with lithologies such as those in our models will fail long before stresses of such high magnitude can accumulate, likely at no more than a few tens of MPa.

[21] The two horizontal stress components differ primarily because of bending that occurs in the smooth plains unit during its contraction. This bending is caused by the non-uniform depth of the fill (i.e., its cross-sectional shape), which in turn is a function of the topography of the basin floor prior to the emplacement of the smooth plains. Figure 4 shows a sampling of the fill geometries considered in our analysis along with the predicted style of faulting. A bowl-shaped fill unit leads to a stress state in which $\sigma_r \approx \sigma_c$ throughout most of the inner smooth plains, with the magnitudes of the two stresses diverging only near the peak ring as a result of thinning of the plains unit (Figure 4a), a stress pattern that would lead to a mix of graben orientations throughout much of the basin interior, including the central region. A fill geometry that thins in a ramp-like or linear fashion from the basin center to the peak ring (Figure 4b) leads to a state in which $\sigma_r > \sigma_c$ throughout the basin and to circumferential graben throughout much of the inner basin, though the most prominent graben are expected to form in the distal parts of the smooth plains. Adopting a flat inner basin floor while retaining the ramp structure at greater radial distances concentrates bending stresses over the ramp
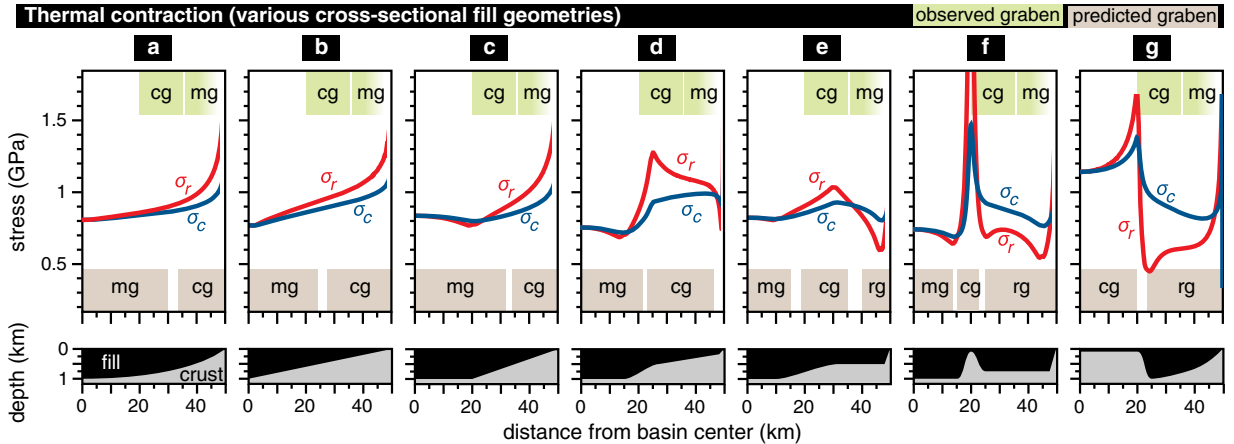
Figure 4. The effects of different fill geometries on the stress state generated in a smooth plains unit during thermal contraction. Each panel shows the circumferential and radial stress components above an illustration of the model's geometry in cross-section, with observed and predicted features shown at the top and bottom edges, respectively; "cg", "rg", and "mg" denote circumferential, radial, and mixed-orientation graben in this figure and in Figures 5, 6, and 7. Vertical stresses are all near zero, because stress values are taken from near the surface of the model (a free surface). Stress magnitudes are in the GPa range, but these values should be regarded only as being supportive of graben formation, because our models do not account for stress relief through faulting.
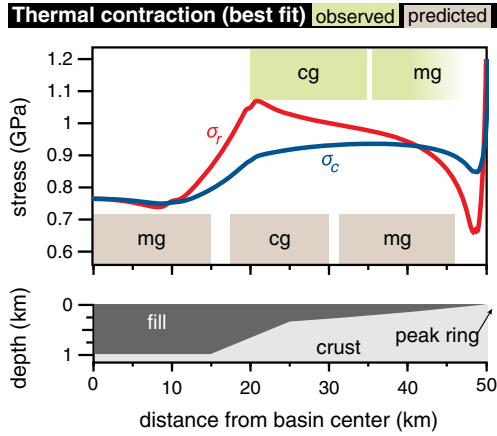
Figure 5. A thermal contraction model that closely matches the pattern of observed graben in the three basins. Observed and predicted features are shown at the top and bottom edges, respectively. This model shows the highest potential for graben formation in the region where the most prominent graben are observed and lower differential stresses immediately inward of the peak ring, where fewer graben are observed.

(Figure 4c), leading to a narrower annular zone of circumferential graben formation. If we also flatten the slope of the outer portion of the subfill basin floor, the resulting stress state is one in which $\sigma_r < \sigma_c$ at radial distances outward of the ramp structure, resulting in a concentration of circumferentially oriented graben at radial distances of ~20–40 km from the basin center (33–66% of r_p), depending on the precise geometry (Figures 4d and 4e).

[22] A geometry that features another, smaller buried basin ring inward of the peak ring (Figure 4f) leads to a stress state that produces a strongly localized region of circumferential graben over that ring. However, such an inner ring has not been observed in any other similarly sized basins on Mercury [e.g., *Baker et al.*, 2012], and so we consider its presence in any of the basins in this study unlikely. We also explored a geometry in which the fill is thinnest at the center of the basin, perhaps due to a buried central peak cluster, in effect testing the idea that a thinner smooth plains unit there might be too thin to form sizeable graben. This geometry produces a similar stress state and pattern of faulting to that of a buried inner ring (Figure 4g), but central peaks and peak clusters are generally associated with much smaller impact craters (typically less than 140 km in diameter) on Mercury [*Baker et al.*, 2011, 2012]. In addition, because vertical contraction of cooling plains material will be greatest where the plains unit is thickest, calculations suggest that any smooth plains that cover a central peak at the center of the basin should have a higher elevation than thicker outer portions of the fill, because they would have subsided less during cooling. Altimeter data, in contrast, show that the floors of these peak-ring basins are lowest at their centers.

[23] Our preferred model is one in which there is a rapid decrease in the thickness of pooled smooth plains material with increasing radius at a distance of ~15 km from the basin center (just inside the onset radius of prominent circumferential graben), and a more gradual decrease in smooth plains thickness from ~25 km radius to the outer edge of the smooth plains (Figure 5). A thermal contraction model with this geometry predicts fault orientations that match the observed circumferential orientations of graben 20–30 km from the basin center as well as the transition to a mix of circumferential and radial graben farther outward. We note, however, that this model predicts the formation of graben at the basin center, where no graben are observed (Figure 1). We address this point in section 5.3.

4.2. Uplift of the Basin Floor

[24] The finite element models for isostatic uplift scenarios began with an initially flat crust–mantle boundary and a basin partially filled with plains material. At the start of each model run we applied a lithostatic state of stress to each element equal to the local overburden. Because the basin is not isostatically compensated by an uplifted crust–mantle boundary, there is an upward body force beneath the basin that must be compensated by a combination of uplift and lithospheric flexural stresses. The flexural wavelength depends in part on lithospheric thickness, so we considered a range of models with an elastic lithosphere thickness ranging from 10 to 100 km under the center of the basin (i.e., 13 to 103 km outside of the basin). We also explored different ratios of the elastic strength of the smooth plains unit to that of the underlying geologic units. That ratio controls how flexural stresses are distributed between plains material and the surrounding crust; a high ratio concentrates stresses within the plains material. We used an elastically weak crust as a proxy for impact-fractured rock with comparatively low yield strength. Our models for this scenario extended to a depth of 200 km (well below the deepest lithosphere–asthenosphere boundary considered in our models) and a radius of 1000 km from the basin center. We placed zero-displacement boundary conditions on the outer and bottom edges of the model and verified that these constraints did not produce a different stress state in the smooth plains than did models with other choices for boundary conditions.

[25] To simulate uplift associated with lower crustal flow, we modified the isostatic uplift model by adding topography on the crust–mantle boundary that fully compensated the effects of basin topography and smooth plains infill. We then included a weak (viscous) lower crustal layer between a strong upper crust and a strong uppermost mantle, both of which were modeled as elastic. We varied the thickness of the crust exterior to the basin between 20 and 80 km (while maintaining isostatic compensation within the basin), and varied the depth of the brittle–ductile transition between 10 and 60 km beneath the basin floor. The mantle underlying this viscous lower crust was assumed to be elastic, to differentiate this model from our models of isostatic uplift. We found that these models produced the same types of stress distributions, and therefore the same predicted styles of faulting in the smooth plains unit, as the isostatic uplift models. For this reason, we discuss both uplift models together.

[26] We find that the largest extensional stresses in uplift models always occur at the basin center, with the relative stress magnitudes ordered to produce graben with predominantly radial orientations, except in the central region where there is no preferred orientation (Figure 6). Regardless of the
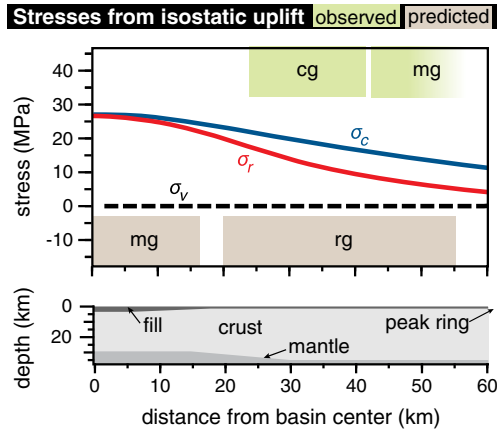
Figure 6. Stress distribution from a model of isostatic uplift. Observed and predicted features are shown at the top and bottom edges, respectively. In this model, the elastic lithosphere is 25 km thick.

choice of model parameters, none of the uplift models predicts the formation of circumferentially oriented graben anywhere within the interior smooth plains. Variations in lithospheric thickness induce changes in the wavelength of the flexural response but do not alter the relative magnitudes or signs of the principal stress components. Similarly, higher ratios between the elastic strength of the smooth plains and the elastic strength of the basement material increase the separation in magnitude between σ_r and σ_c away from the basin center but do not change the predicted graben orientations.

[27] Uplift models not only result in a stress state that does not match observed faulting patterns, they present timing issues that make them an unlikely mechanism for graben formation in the peak-ring basins of this study. For basin uplift to be the principal mechanism for the formation of graben, interior smooth plains would have to have been emplaced and substantially cooled prior to the onset of uplift. If the smooth plains in all three basins formed from impact melts, such a timing constraint might be satisfied. To the extent that interior smooth plains are volcanic in origin, however, they had to have been emplaced sufficiently soon after basin formation to have solidified earlier than much of the isostatic uplift or lower crustal flow. As the smooth plains within Rachmaninoff have a resolvably younger age than the basin on the basis of crater size-frequency distributions and color differences [*Prockter et al.*, 2010; *Chapman et al.*, 2012], and as uplift would have occurred shortly after basin formation by the mechanisms considered here (e.g., within perhaps 10 kyr to 1 Myr, depending on the viscosity of lower crust or upper mantle) neither uplift mechanism is likely to have been the source of graben formation in the smooth plains unit in that basin.
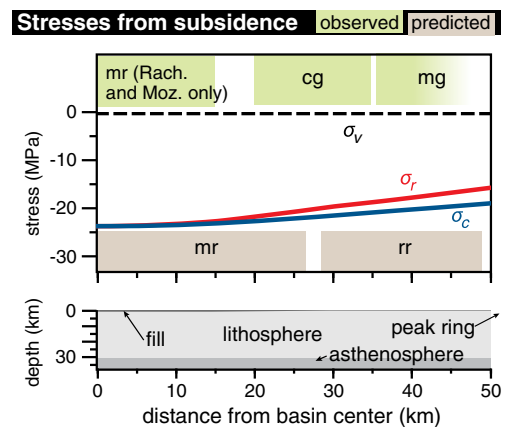
4.3. Subsidence Due to Volcanic Loading

[28] Volcanic loading models include topography on the crust–mantle boundary and an initial lithostatic state of stress corresponding to full isostatic compensation of basin topography prior to interior smooth plains emplacement. The addition of smooth plains material and the application of gravity to the model then induces lithospheric subsidence in response to the uncompensated volcanic load. Models

were run until the asthenosphere reached complete relaxation, at which point the volcanic load was supported by isostatic forces and lithospheric flexural stresses. The flexural wavelength (and therefore the location of the annular flexural bulge) is influenced by both the shape of the volcanic load and the thickness of the lithosphere, so we considered models with several different load geometries and different assumed values for the thickness of the elastic lithosphere ranging from 10 to 100 km (i.e., 13 to 103 km outside the basin). Crustal thickness was varied between 20 and 80 km outside the basin, with a thickness inside the basin determined by isostatic compensation prior to volcanic infill. Model domain, mesh resolution, and boundary conditions were similar to those used for models of isostatic uplift.

[29] For all subsidence models considered, the flexural wavelength is sufficiently large that the entire smooth plains unit within the basin is in compression, precluding the formation of interior graben (Figure 7). The geometry of the load has very little effect on the distribution of stresses, especially for the larger values of lithosphere thickness, and the same is true for the ratio of the elastic strength of the smooth plains to that of underlying units.

[30] Subsidence models can account for the presence of irregularly oriented ridges at the centers of Rachmaninoff and Mozart, as all of these flexural models result in a stress state in which σ_r and σ_c are compressional and approximately equal at the basin center. It is not obvious why ridges would develop only in the very center of the basins, however, as the decrease in compressional stresses outward from the basin center is gradual (Figure 7). We speculate that compressive stresses at the basin center were barely sufficient to initiate ridge formation, so that even a gradual outward decrease in the magnitude of such stresses prevented contractional strain from developing farther from the basin center. This scenario would be aided by the relaxation of compressional stresses that would accompany the formation of the central ridges, further lowering compressional stresses beyond the basin center. The concept that ridges at the

Figure 7. Stress distribution from a model of subsidence in response to volcanic loading. Observed and predicted features are shown at the top and bottom edges of the stress plot, respectively; as in Figure 4, "cg", "rg", and "mg" denote circumferential, radial, and mixed-orientation graben, and "rr" and "mr" denote radial ridges and mixed-orientation ridges. In this model the elastic lithosphere is 30 km thick.
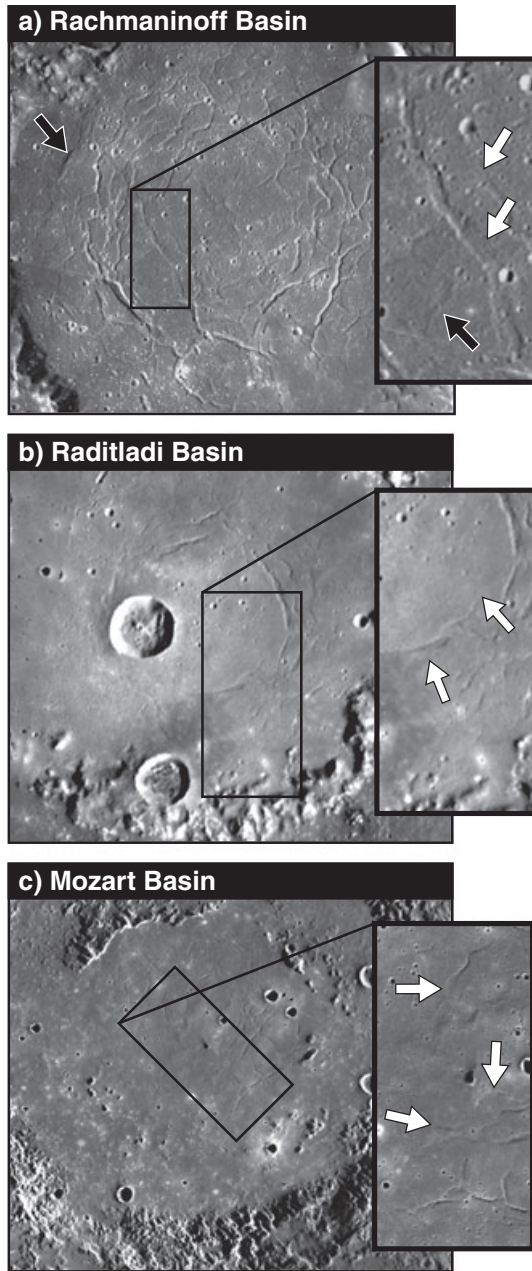
Figure 8. Evidence for graben partially filled by volcanic flows (a) southwest of the center of Rachmaninoff basin, (b) southeast of the center of Raditladi basin, and (c) south of the center of Mozart basin, from MDIS narrow-angle image mosaics at 150 m pixel^{-1}. Black rectangles in larger images indicate the areas shown in the expanded views, and white arrows point to areas where graben are seen either to terminate abruptly or to shoal with no change in width. The black arrow in (a) points to the ridge discussed in section 4.3.

age. The topography of the basins (e.g., Figures 1g, 1h, and 1i) also supports this idea. The profile for Rachmaninoff displays the greatest relief of the three basins, and it also has the most extensive ridge system, whereas the lesser relief in Raditladi may indicate that it has undergone less subsidence.

[31] Ridge formation may have also been aided by the long-term accumulation of compressional stresses that accompanied cooling of Mercury's interior and associated global contraction [*Strom et al.*, 1975; *Solomon*, 1977]. This source of compressional stress may have played a role in the formation of at least two ridges observed far from the basin center in Rachmaninoff (Figure 1d and black arrows in Figure 8a).

5. Discussion

[32] The thermal contraction of volcanic fill provides the most likely explanation for the formation of graben in the Rachmaninoff, Raditladi, and Mozart basins. Finite element models of that process are able to reproduce most aspects of the observed patterns of faulting. In contrast, neither uplift nor subsidence scenarios can match the observed graben distribution. This conclusion, in turn, supports the notion that the smooth plains within the peak rings of these three basins are volcanic in origin, corroborating independent evidence for such an origin for the inner plains in Rachmaninoff and Mozart. It also supports a volcanic origin for the smooth plains in Raditladi, as it seems unlikely that a similar pattern of faulting would be produced from the cooling of both impact melt and volcanic deposits due to their different cross-sectional shapes. The inference that thermal contraction of a volcanic unit produced the observed features carries with it some implications for the origin of the materials filling the basin and for the region's associated volcanic history, as discussed below (see sections 5.2 and 5.3). The ridges found at the center of the Rachmaninoff and Mozart basins also warrant additional discussion (see section 5.3).

5.1. Implications of Thermal Contraction: A Step in the Sub-Volcanic Basin Floor

[33] The models for thermal contraction that best match the observed pattern of graben feature a rapid decrease in the thickness of smooth plains material between 15 km and 20 km radius (25–33% of r_p). Such an inferred geometry finds some support in observations of, and model results for, other peak-ring basins. For example, hydrocode simulations of the formation of craters of diameter $D \sim 200$ km suggest that a central area of the final basin is deeper than the area near the peak ring and that there is a relatively abrupt transition in depth [*Collins et al.*, 2002]. A similar central deepening appears to be present in the Mead crater on Venus ($D \sim 270$ km), although it is unclear if that depression could have been caused by post-volcanic-fill processes, as that basin contains a system of disorganized central faulting [*Alexopoulos and McKinnon*, 1992; *Herrick and Sharpton*, 1996; *Stoddard and Jurdy*, 2006]. The central deepening also appears in the largely unfilled multiring Orientale basin on the Moon ($D \sim 950$ km) [e.g., *Whitten et al.*, 2011], further supporting the possibility that such a geometry might apply beneath the plains material in Mercury's peak-ring basins. The applicability of this geometry to the few unfilled peak-ring basins on Mercury remains to be explored.

centers of the Rachmaninoff and Mozart basins formed in response to compressive stresses just sufficient to initiate deformation is consistent with the lack of central ridges observed in Raditladi, if the latter basin experienced somewhat less subsidence due to its lesser amount of fill or its younger

5.2. Implications of Thermal Contraction: A Thick Volcanic Cooling Unit

[34] Graben formation from thermal contraction implies a relatively thick (at least 1 km) cooling unit, a result consistent with the ~1.5 km thickness of volcanic plains inferred from the depth extent of graben-bounding faults in Mercury's northern plains [*Klimczak et al.*, 2012]. The volcanic materials that partially filled these basins need not have been emplaced in a single event, however. A series of thinner flows could also form a thick unit, as long as those flows occurred in sufficiently rapid succession (~thousands of years or less) that no layer is able to cool substantially below the elastic blocking temperature before the next one above it is emplaced [*Freed et al.*, 2012]. Whether the smooth plains units within the basins of this study represent a series of thin flows or a single, very voluminous flow, the implication is one of high effusion rates and low viscosities. Both of these properties are suggested for the lavas that flooded Mercury's northern plains [*Head et al.*, 2011] and that helped to shape adjoining areas [*Byrne et al.*, 2012]. Without these characteristics, the flows would not likely have been able to build the thick and generally axisymmetric units that produced the distribution of graben in Rachmaninoff, Raditladi, and Mozart.

[35] In contrast, the lunar Schrödinger basin provides an example of a basin in which interior volcanic plains vary in both texture and albedo, suggesting episodic flows that cooled at different times [*Mest*, 2011]. The Schrödinger basin does contain several very large graben, but they occur in an asymmetric pattern that cuts across both the peak ring and the basin rim and are individually much longer than the graben observed in Rachmaninoff, Raditladi, and Mozart basins, with some in excess of 100 km in length [e.g., *Shoemaker et al.*, 1994]. These observations suggest that graben formed within the Schrödinger basin as the result of a regional-scale process, possibly associated with uplift [*Shoemaker et al.*, 1994], rather than as a product of local thermal contraction.

5.3. Implications of Thermal Contraction: Late-Stage Volcanic Flows

[36] The thermal contraction model predicts that graben should have formed at the centers of the Rachmaninoff, Raditladi, and Mozart basins, where no graben are observed (Figure 1). Contractional features are seen in the central areas of two of the basins, but ridge formation would not have removed evidence for earlier graben, as cross-cutting ridges and graben are commonly observed in lunar basins (e.g., Orientale and Serenitatis) [*Solomon and Head*, 1980] and in the Caloris and Rembrandt basins on Mercury. One could surmise that if compressional stresses associated with subsidence of the basin center developed at the same time that the volcanic fill was thermally contracting, the compressional stresses could have prevented the extensional stress state necessary for graben formation from developing at the basin center. However, the magnitude of extensional thermal stresses (Figure 5) is more than a factor of 50 greater than the magnitude of compressional stresses due to subsidence (Figure 7), suggesting that subsidence-induced stresses would not have been sufficient to prevent graben formation.

[37] A more likely scenario is that graben in the centers of the three peak-ring basins were buried by one or more thin, late-stage lava flows. The late flow or flows in each basin would have to have been sufficiently voluminous to fill the central graben but sufficiently thin not to form new graben during cooling. The timing for the emplacement of such late-stage flows is flexible, constrained only by the need for such flows to have been emplaced after the primary smooth plains unit had cooled below the elastic blocking temperature (~20 kyr for a 1 km thick smooth plains unit). It might also be inferred that these late-stage flows occurred at the end of the phase of volcanism that generated the plains in which graben formed, on the grounds that the central areas in these basins do not have resolvable differences from the surrounding smooth plains in terms of spectral reflectance, age, or morphology. The late-stage flow hypothesis suggests that the observed ridges formed after cessation of volcanism and are therefore younger than the graben, though the partial or complete burial of an earlier stage of ridges cannot be ruled out. The observation that some of the innermost graben display less distinct edges and shorter shadows than those of the more prominent graben farther from the basin centers also supports the hypothesis of late-stage flows and partial volcanic burial of the central areas (Figure 8). Higher-resolution images of the central regions of these basins will permit more rigorous tests of this hypothesis.

[38] Other possible indications of late-stage flows are areas in these three basins where the distribution of graben is discontinuous. These areas generally correspond to sectors where portions of the peak ring are missing, suggesting that volcanic resurfacing may be responsible for both sets of observations. This effect is most apparent in the southwestern quadrants of Raditladi (Figure 1e) and Mozart (Figure 1f). This scenario supports a volcanic origin for at least a portion of the smooth plains in Raditladi. Source vents for late-stage volcanism could have been in either the outer or inner portion of the basins, though inward flow seems more likely given evidence from altimetry that the centers are at the lowest modern elevation in each of these basins (Figures 1g, 1h, and 1i). In Raditladi, ejecta from a prominent younger crater in this region may have also contributed to graben burial. Both the peak ring and the graben pattern are largely uninterrupted in Rachmaninoff. For the late-stage flow scenario to apply to this basin, a central source vent would be the most straightforward explanation. Although greater subsidence and associated compressional stresses at the basin center might be expected to suppress magma ascent, a centrally sourced late-stage flow could have predated most subsidence. As noted in section 2.2, the relative timing of the formation of the basin-central ridges and the surrounding graben is unconstrained.

6. Conclusions

[39] From observations of fault patterns within the Rachmaninoff, Raditladi, and Mozart basins on Mercury, we have inferred the state of stress at the time of faulting, and we have tested several candidate processes (thermal contraction, uplift, and volcanic loading) by comparing their predicted states of stress to those inferred from observations. Our finite element model results suggest that thermal contraction of a

volcanic smooth plains unit is the most likely mechanism for forming the observed patterns of graben. Our models also predict that graben should have formed in the centers of the basins, though no such features are observed. We suggest that such graben were covered by thin, late-stage flows of volcanic material. Some evidence for such late-stage flows may be seen in the form of partially buried graben and in spatial correlations between missing sections of peak ring and areas that are devoid of graben.

[40] Several implications follow from aspects of the models that best match observations: (1) the basin floor prior to volcanic infill was deeper beneath the basin center than it was farther out toward the peak ring; (2) the inner smooth plains in all three basins are volcanic in origin; and (3) the smooth plains cooling unit was ~1 km thick, supporting the hypothesis that many volcanic flows on Mercury were characterized by high effusion rates and low viscosities.

[41] Neither uplift associated with isostatic adjustment or lower crustal flow nor subsidence associated with lithospheric loading can account for the observed graben, but the latter process likely contributed to the formation of ridges in the centers of Rachmaninoff and Mozart basins. Compression associated with global contraction may have been another contributor to ridge formation.

[42] Our results support the idea that the distribution of tectonic features in the Rachmaninoff, Raditladi, and Mozart basins on Mercury differs from patterns of tectonic features in Schrödinger basin on the Moon primarily because of the thickness of the youngest major volcanic unit. The faulting that results from thermal contraction is sensitive to fill thickness and geometry, so the formation of sets of concentric graben, rather than pervasive cracking, requires that the cooling volcanic unit be emplaced approximately axisymmetrically and sufficiently rapidly to cool as a single body. If volcanic flows on Mercury commonly involved the rapid emplacement of large volumes of highly fluid lava, thus enabling the formation of concentric graben, then by contrast the effusion rates for mare basaltic lavas on the Moon must have generally been too low for these distinctive graben patterns to develop.

References

Ahrens, T. J. (Ed.) (1995), *Rock Physics & Phase Relations: A Handbook of Physical Constants*, *AGU Reference Shelf*, vol. 3, 236 pp., AGU, Washington, D.C., doi:10.1029/RF003.

Alexopoulos, J. S., and W. B. McKinnon (1992), Multiringed impact craters on Venus: An overview from Arecibo and Venera images and initial Magellan data, *Icarus*, *100*, 347–363.

Anderson, E. M. (1951), *The Dynamics of Faulting*, Oliver and Boyd, Edinburgh, 206 pp.

Andrews-Hanna, J. C., M. T. Zuber, and S. A. Hauck II (2008), Strike-slip faults on Mars: Observations and implications for global tectonics and geodynamics, *J. Geophys. Res.*, *113*, E08002, doi:10.1029/2007JE002980.

Baker, D. M. H., J. W. Head, S. C. Schon, C. M. Ernst, L. M. Prockter, S. L. Murchie, B. W. Denevi, S. C. Solomon, and R. G. Strom (2011), The transition from complex crater to peak-ring basin on Mercury: New observations from MESSENGER flyby data and constraints on basin

formation models, *Planet. Space Sci.*, *59*, 1932–1948, doi:10.1016/J.PSS.2011.05.010.

Baker, D. M. H., et al. (2012), New morphometric measurements of peak-ring basins on Mercury and the Moon: Results from the Mercury Laser Altimeter and Lunar Orbiter Laser Altimeter, *Lunar Planet. Sci.*, *43*, abstract 1238.

Banerdt, W. B., M. P. Golombek, and K. L. Tanaka (1992), Stress and tectonics on Mars, in *Mars*, edited by H. H. Kieffer, B. M. Jakosky, C. W. Snyder, and M. S. Matthews, pp. 249–297, University of Arizona Press, Tucson, Ariz.

Barnouin, O. S., M. T. Zuber, D. E. Smith, G. A. Neumann, R. R. Herrick, J. E. Chappelow, S. L. Murchie, and L. M. Prockter (2012), The morphology of craters on Mercury: Results from the MESSENGER flybys, *Icarus*, *219*, 414–427, doi:10.1016/J.ICARUS.2012.02.029.

Byrne, P. K., C. Klimczak, D. A. Williams, D. M. Hurwitz, S. C. Solomon, J. W. Head, F. Preusker, and J. Oberst (2012), An assemblage of lava flow features on Mercury, *J. Geophys. Res.*, submitted.

Chapman, C. R., W. J. Merline, S. Marchi, L. M. Prockter, C. I. Fassett, J. W. Head, S. C. Solomon, and Z. Xiao (2012), The young inner plains of Mercury's Rachmaninoff basin reconsidered, *Lunar Planet. Sci.*, *43*, abstract 1607.

Collins, G. S., H. J. Melosh, J. V. Morgan, and M. R. Warner (2002), Hydrocode simulations of Chicxulub crater collapse and peak-ring formation, *Icarus*, *157*, 24–33, doi:10.1006/ICAR.2002.6822.

Denevi, B. W., et al. (2009), The evolution of Mercury's crust: A global perspective from MESSENGER, *Science*, *324*, 613–618, doi:10.1126/science.1172226.

Dyksterhuis, S., R. D. Müller, and R. A. Albert (2005), Paleostress field evolution of the Australian continent since the Eocene, *J. Geophys. Res.*, *110*, B05102, doi:10.1029/2003JB002728.

Dzurisin, D. (1978), The tectonic and volcanic history of Mercury as inferred from studies of scarps, ridges, troughs, and other lineaments, *J. Geophys. Res.*, *83*, 4883–4906.

Fassett, C. J., et al. (2012), Large impact basins on Mercury: Global distribution, characteristics, and modification history from MESSENGER orbital data, *J. Geophys. Res.*, *117*, E00L08, doi:10.1029/2012JE004154.

Freed, A. M., H. J. Melosh, and S. C. Solomon (2001), Tectonics of mascon loading: Resolution of the strike-slip faulting paradox, *J. Geophys. Res.*, *106*, 20,603–20,620.

Freed, A. M., T. Herring, and R. Bürgmann (2010), Steady-state laboratory flow laws alone fail to explain postseismic observations, *Earth Planet. Sci. Lett.*, *300*, 1–10, doi:10.1016/j.epsl.2010.10.005.

Freed, A. M., D. M. Blair, T. R. Watters, C. Klimczak, P. K. Byrne, S. C. Solomon, M. T. Zuber, and H. J. Melosh (2012), On the origin of graben and ridges within and near volcanically buried craters and basins in Mercury's northern plains, *J. Geophys. Res.*, *117*, E00L06, doi:10.1029/2012JE004119.

Golombek, M. P., and R. J. Phillips (2010), Mars tectonics, in *Planetary Tectonics*, edited by T. R. Watters and R. A. Schultz, Cambridge University Press, Cambridge.

Hauck, S. A., II, A. J. Dombard, R. J. Phillips, and S. C. Solomon (2004), Internal and tectonic evolution of Mercury, *Earth Planet. Sci. Lett.*, *222*, 713–728, doi:10.1016/j.epsl.2004.03.037.

Head, J. W., et al. (2011), Flood volcanism in the northern high latitudes of Mercury revealed by MESSENGER, *Science*, *333*, 1853–1856, doi:10.1126/science.1211997.

Herrick, R. R., and V. L. Sharpton (1996), Geologic history of the Mead impact basin, Venus, *Geology*, *24*, 11–14.

Hirth, G. (2002), Laboratory constraints on the rheology of the upper mantle, *Rev. Mineral. Geochem.*, *51*, 97–120, doi:10.2138/GSRMG.51.1.97.

Kennedy, P. J., A. M. Freed, and S. C. Solomon (2008), Mechanisms of faulting in and around Caloris basin, Mercury, *J. Geophys. Res.*, *113*, E08004, doi:10.1029/2007JE002992.

Klimczak, C., T. R. Watters, C. M. Ernst, A. M. Freed, P. K. Byrne, S. C. Solomon, D. M. Blair, and J. W. Head (2012), Deformation associated with ghost craters and basins in volcanic smooth plains on Mercury: Strain analysis and implications for plains evolution, *J. Geophys. Res.*, *117*, E00L03, doi:10.1029/2012JE004100.

Martellato, E., M. Massironi, G. Cremonese, S. Marchi, S. Ferrari, and L. M. Prockter (2010), Age determination of Raditladi and Rembrandt basins and related geological units, *Lunar Planet. Sci.*, *41*, abstract 2148.

Melosh, H. J. (1978), Tectonics of mascon loading, *Proc. Lunar Planet. Sci. Conf. 9th*, 3513–3525.

Melosh, H. J., and D. Dzurisin (1978), Tectonic implications for gravity structure of Caloris basin, Mercury, *Icarus*, *33*, 141–144.

Melosh, H. J., and W. B. McKinnon (1988), The tectonics of Mercury, in *Mercury*, edited by F. Vilas, C. R. Chapman, and M. S. Matthews, pp. 374–400, University of Arizona Press, Tucson, Ariz.

Melosh, H. J., and C. A. Williams Jr. (1989), Mechanics of graben formation in crustal rocks: A finite element analysis, *J. Geophys. Res.*, *94*, 13,961–13,973.

Mest, S. C. (2011), The geology of Schrödinger basin: Insights from post-Lunar Orbiter data, in *Recent Advances and Current Research Issues in Lunar Stratigraphy*, edited by W. A. Ambrose and D. A. Williams, Special Paper 477, pp. 95–115, Geological Society of America, Boulder, Colo., doi:10.1130/2011.2477(04).

Nittler, L. R., et al. (2011), The major-element composition of Mercury's surface from MESSENGER X-ray spectrometry, *Science*, *333*, 1847–1850, doi:10.1126/science.1211567.

Poulet, T., A. Karrech, K. Regenauer-Lieb, L. Fisher, and P. Schaubs (2012), Thermal-hydraulic-mechanical-chemical coupling with damage mechanics using ESCRIPTRT and ABAQUS, *Tectonophysics*, *526-529*, 124–132, doi:10.1016/J.TECTO.2011.12.005.

Preusker, F., J. Oberst, J. W. Head, T. R. Watters, M. S. Robinson, M. T. Zuber, and S. C. Solomon (2011), Stereo topographic models of Mercury after three MESSENGER flybys, *Planet. Space Sci.*, *59*, 1910–1917, doi:10.1016/J.PSS.2011.07.005.

Prockter L. M., et al. (2009), The curious case of Raditladi basin, *Lunar Planet. Sci.*, *40*, abstract 1758.

Prockter, L. M., et al. (2010), Evidence for young volcanism on Mercury from the third MESSENGER flyby, *Science*, *329*, 668–671, doi:10.1126/science.1188186.

Prockter, L. M., D. M. H. Baker, J. W. Head, S. L. Murchie, C. M. Ernst, C. R. Chapman, B. W. Denevi, S. C. Solomon, T. R. Watters, and M. Massironi (2011), The geology of medium-sized impact basins on Mercury, *Abstracts with Programs, 43*, paper 142-11, p. 359, Geological Society of America, Boulder, Colo.

Schultz, R. A., and M. T. Zuber (1994), Observations, models, and mechanisms of failure of surface rocks surrounding planetary surface loads, *J. Geophys. Res.*, *99*, 14,691–14,702.

Schultz, R. A., J. M. Moore, E. B. Grosfils, K. L. Tanaka, and D. Mége (2007), The Canyonlands model for planetary grabens: Revised physical basis and implications, in *The Geology of Mars: Evidence from Earth-Based Analogs*, edited by M. Chapman, pp. 371–399, Cambridge University Press.

Schultz, R. A., R. Soliva, C. H. Okubo, and D. Mege (2010), Fault populations, in *Planetary Tectonics*, edited by T. R. Watters and R. A. Schultz, Cambridge University Press, Cambridge.

Shoemaker, E. M., M. S. Robinson, and E. M. Eliason (1994), The south pole region of the Moon as seen by Clementine, *Science*, *266*, 1851–1854.

Solomon, S. C. (1977), The relationship between crustal tectonics and internal evolution in the Moon and Mercury, *Phys. Earth Planet. Inter.*, *15*, 135–145.

Solomon, S. C., and J. W. Head (1979), Vertical movement in mare basins: Relation to mare emplacement, basin tectonics, and lunar thermal history, *J. Geophys. Res.*, *84*, 1667–1682.

Solomon, S. C., and J. W. Head (1980), Lunar mascon basins: Lava filling, tectonics, and evolution of the lithosphere, *Rev. Geophys.*, *18*, 107–141.

Solomon, S. C., et al. (2008), Return to Mercury: A global perspective on MESSENGER's first Mercury flyby, *Science*, *321*, 59–62, doi:10.1126/science.1159706.

Stoddard, P. R., and D. M. Jurdy (2006), Comparison of topographic profiles across Venus' coronae and craters: Implications for corona origin hypothesis, *Eos Trans. AGU*, *87*(52), Fall Meeting Suppl., abstract P51B-1199.

Strom, R. G., N. J. Trask, and J. E. Guest (1975), Tectonism and volcanism on Mercury, *J. Geophys. Res.*, *80*, 2478–2507.

Vasavada, A. R., D. A. Paige, and S. E. Wood (1999), Near-surface temperatures on Mercury and the Moon and the stability of polar ice deposits, *Icarus*, *141*, 179–193.

Watters, T. R., F. Nimmo, and M. S. Robinson (2005), Extensional troughs in the Caloris basin of Mercury: Evidence of lateral crustal flow, *Geology*, *33*, 669–672, doi:10.1130/G21678.1.

Watters, T. R., S. C. Solomon, M. S. Robinson, J. W. Head, S. L. André, S. A. Hauck II, and S. L. Murchie (2009a), The tectonics of Mercury: The view after MESSENGER's first flyby, *Earth Planet. Sci. Lett.*, *285*, 283–296, doi:10.1016/j.epsl.2009.01.025.

Watters, T. R., S. L. Murchie, M. S. Robinson, S. C. Solomon, B. W. Denevi, S. L. André, and J. W. Head (2009b), Emplacement and tectonic deformation of smooth plains in the Caloris basin, Mercury, *Earth Planet. Sci. Lett.*, *285*, 309–319, doi:10.1016/j.epsl.2009.03.040.

Watters, T. R., J. W. Head, S. C. Solomon, M. S. Robinson, C. R. Chapman, B. W. Denevi, C. I. Fassett, S. L. Murchie, and R. G. Strom (2009c), Evolution of the Rembrandt impact basin on Mercury, *Science*, *324*, 618–621, doi:10.1126/science.1172109.

Watters, T. R., S. C. Solomon, C. Klimczak, A. M. Freed, J. W. Head, C. M. Ernst, M. S. Robinson, D. M. Blair, T. A. Goudge, and P. K. Byrne (2012), Extension and contraction within volcanically buried impact craters and basins on Mercury, *Geology*, *12*, 11–23, doi:10.1130/G33725.

Whitten, J. W., J. W. Head, M. Staid, C. M. Pieters, J. Mustard, R. Clark, J. Nettles, R. L. Klima, and L. Taylor (2011), Lunar mare deposits associated with the Orientale impact basin: New insights into mineralogy, history, mode of emplacement, and relation to Orientale Basin evolution from Moon Mineralogy Mapper (M3) data from Chandrayaan-1, *J. Geophys. Res.*, *116*, E00G09, doi:10.1029/2010JE003736.

Zhong, S. (1997), Dynamics of crustal compensation and its influences on crustal isostasy, *J. Geophys. Res.*, *102*, 15,287–15,299.

Zuber, M. T., et al. (2010), Accommodation of lithospheric shortening on Mercury from altimetric profiles of ridges and lobate scarps measured during MESSENGER flybys 1 and 2, *Icarus*, *209*, 247–255, doi:10.1016/J.ICARUS.2010.02.026.